Electronic density corrugation and crystal azimuthal orientation effects on energy losses of hydrogen ions in grazing scattering on a Ag(110) surface

J. E. Valdés,[1,*] P. Vargas,[1] C. Celedón,[1] E. Sánchez,[2] L. Guillemot,[3] and V. A. Esaulov[3]
[1]*Atomic Collision Laboratory, Physics Department, Universidad Técnica Federico Santa María, Valparaíso, Casilla 110-V, Chile*
[2]*Centro Atómico Bariloche, Atomic Collisions Division, CNEA, and CONICET, 8400 San Carlos de Bariloche, Río Negro, Argentina*
[3]*Laboratoire des Collisions Atomiques et Moléculaires (Unité Mixte de Recherche UMR 8625), bât 351, Université de Paris Sud, Orsay 91405, France*
(Received 19 February 2008; published 15 September 2008)

We present a detailed study of the energy losses of hydrogen ions that are scattered off an Ag(110) single-crystal surface for primary energies between 1 and 4 keV. We performed measurements for grazing angles as a function of crystal azimuthal orientation, which show large differences in energy losses. Experimental results are discussed by means of trajectory calculations of protons scattered under grazing-incidence conditions on the surface. Using nonlinear models for the stopping power, *ab initio* crystal structure calculations of the electronic density, and semiclassical simulations, we obtain data that are in very good agreement with experimental results. These simulations allow us to properly take into account the variations of the surface electronic density and hence obtain an accurate description of the energy loss processes for ion scattering along various azimuthal orientations of the target.

DOI: 10.1103/PhysRevA.78.032902 PACS number(s): 03.67.Lx, 34.50.Bw, 79.20.Rf

I. INTRODUCTION

The stopping of ions in matter has attracted much attention both theoretically and experimentally. From a practical point of view, this subject is of interest in a number of areas such as semiconductor doping using ion beams or ion-beam cancer treatment. In all these cases an accurate knowledge of the penetration depth of ions in matter is necessary. Many studies have focused on charged particle penetration of bulk matter [1–3] and for polycrystalline materials. In the case of monocrystalline solids, the situation is complicated by channeling effects. Similarly, in the case of surface scattering, the phenomenon is also complex. This is because regions far from the first atomic layer, where the electronic density decreases, may contribute to energy losses. The trajectory lengths depend on the scattering conditions, like incident and azimuthal angles, and very different trajectory types can be found. Several recent experimental and theoretical investigations have focused on these problems [4–11], but the stopping of ions along different crystallographic orientations on the surface, where strong corrugations of the electron density are observed, was not adequately described. This is related to the fact that at a given distance from the surface, an averaged electron density was assumed (see, e.g., [11]), which does not realistically describe the density corrugation above a crystal, especially in directions with high symmetry.

In the present paper, we report results of an investigation of the energy losses of low-energy hydrogen ions scattered under grazing incidence on an Ag(110) surface for various crystalline directions. In an attempt to rationalize our experimental findings, we have performed semiclassical and deterministic simulations for particles under the same type of conditions as the experimental one. We follow an approach developed by us previously [13] for passage of ions through thin foils and scattering on surfaces and which we now improve. In these calculations we solve the Newton equation for the particle under the influence of the forces due to the nuclei and core electrons and the stopping force coming from elastic and inelastic interaction. The former forces influence the multiple-scattering processes. For the case of noble metals like Ag and Au, proper inclusion of all valence electrons (s, p, and also d) is important, as we have discussed previously [12] and has been pointed out very recently [14]. In our approach we include a quantum dissipative friction force resulting from the interaction with the valence electrons (s, p, and d), and we use a nonlinear model and the local density approximation [12–14]. With this friction force we describe the electronic energy loss and energy loss straggling processes for the ions at the surface and inside the solid at the first atomic layers. An important feature is added to our calculations and corresponds to the so called "threshold effect" for the excitation of valence electrons, as described in [12,13].

On the other hand, in order to obtain the energy loss and scattering parameters we need to characterize the surface and bulk of the crystalline target with its spatial atomic positions and spatial valence electronic density. The spatial electron density is obtained through first-principles calculations [15,16].

With this description of the target and semiclassical simulations of the projectile dynamics, we can obtain the ion trajectories and study the differences induced by lattice steering effects in the energy loss distributions. As opposed to approaches used in earlier works [8,9,11], these calculations allow us to properly take into account the spatial inhomogeneity of the surface electronic density and hence obtain a more accurate description of the energy loss processes for ion scattering along various azimuthal orientations of the target.

The experiments and calculations will be described in the next sections. We use atomic units throughout this paper unless otherwise specified.

*Corresponding author. jorge.valdes@usm.cl

II. EXPERIMENT

A brief account of some of the experiments we performed is given in an earlier work [11]. The measurements were performed using an experimental apparatus described in detail elsewhere [17]. Briefly, H^+ or H^- ions are produced in a discharge source using H_2 gas. The ions are mass selected and deflected through 90° to eliminate photons and neutrals before entering into the main UHV chamber. The pressure in the chamber is of typically 2×10^{-10} Torr. The apparatus is equipped for measurement of ion energy spectra using an energy analyzer, as well as time-of-flight (TOF) scattering and direct-recoil spectroscopy.

The Ag samples were bought polished to 0.05 μm. *In situ* preparation consisted of repeated cycles of small-angle (a few degrees, usually less than 3.5°) Ar^+ sputtering and annealing. During sputtering, the crystal was rotated in order to avoid induction of structures due to sputtering and obtain a flat surface. In an earlier work [17] we have shown that this procedure yields results for H^- ion fractions, which are very sensitive to residual surface roughness, in excellent agreement with theory. The surface cleanliness was ascertained by measuring TOF spectra of scattered and recoiled particles under Ar bombardment. The surface was assumed to be cleaned when statistically significant peaks of recoiled O and H were no longer observed.

Scattering measurements were mainly made using a TOF technique for ion energies in the 1–4-keV range for a scattering angle of 7° using a position-sensitive 30-mm-diameter channel-plate multi-anode detector set at a distance of 2.2 m from the scattering center at the end of a TOF analysis tube. A deflector plate assembly set before the channel plate allows separating the incoming positive and negative ions and neutrals, which can thus be detected simultaneously by three anodes. The detecting system has an acceptance angle of about 0.08° in the (horizontal) scattering plane and 0.2° in the out-of-plane (vertical) direction. The incident-beam maximum divergence as defined by collimation slits is $\pm0.2°$ in the scattering plane.

Measurements were made for specular scattering conditions with an incident angle of 3.5° as measured with respect to the surface plane. The target angular position is determined by controlling the ion current and wobbling (rotating) the target slightly. Subsequently a maximum count rate at the detector may be sought to check the optimal counting position. The incident angle is therefore defined to an accuracy of about 0.1°. Time-of-flight spectra for each charge state were recorded. In these measurements the energy losses are determined with respect to the energy of the incident beam electrically reflected from the sample. This corresponds to scattering with a repulsive voltage applied to the sample so that the ions do not undergo any inelastic processes.

The crystal azimuthal setting is determined by measuring the scattered intensity of the ion beam in the forward direction during an azimuthal scan. This allows a precision better than 0.2°. In the following we will refer to the crystal azimuth in terms of angles in degrees counted from the {001} direction; i.e., 0° refers to the {001} direction and 90° refers to the $\{1^-1\ 0\}$ direction.

III. SURFACE AND BULK ELECTRON DENSITY

In order to describe the electronic density of surface and bulk in real space retaining their inhomogeneities, we have performed detailed calculations of the Ag(110) system. Our description is based on the *ab initio* linear muffin-tin orbital (LMTO) method, which has been explained elsewhere [12,13,15,16]. The method is based on density functional theory (DFT) within the local density approximation (LDA) for the exchange correlation potential. The calculation solves iteratively the Kohn-Sham equations taking into account the spatial environment of the atoms until self-consistency is reached. The charge densities using this method are in excellent agreement with those obtained from linear augmented plane-wave full-potential (LAPW) calculations, although the LMTO method uses an atomic sphere approximation for the one-electron potential and empty spheres to simulate the interstitial region in open structures [16]. To model our system, we have used a rectangular supercell $(2d\times\sqrt{2}d\times10d)$, where $d=a/\sqrt{2}$, a being the standard lattice constant for silver ($a=4.086$ Å). This cell contains 20 atoms including the empty interstitial spheres. In the z direction ($\langle110\rangle$ direction), there are 20 atomic planes within a distance of $10d$; of them, 8 atomic planes were left empty in order to simulate the surface, as shown in Fig. 1. In this figure we show also the electronic density profile averaged in the XY plane as a function of the z coordinate. This calculation was done gradually by calculating the electronic charge density profile along the z direction and, in this way, estimating the separation between the slabs. The charge density in the middle of the empty region was less than 1×10^{-6} in a.u. The atomic sphere radii used were 3.167 Å for Ag and 2.761 Å for the interstitial spheres.

In order to get an idea about the different contribution of s, p, and d electrons of the valence band, we show in Fig. 2 the charge density (angular average) variation with distance from the atom position in bulk and surface. The electronic charge density is predominantly of d character in both cases. The s and p contributions are important only in the interstitial regions.

The XY dependence of the spatial variation of the electronic charge density is illustrated in Fig. 3 for the bulk and surface, respectively. Figure 3(a) shows the average density profile projection of the valence charge density in the $\langle110\rangle$ plane in a.u. at 0.72 Å above the first atomic layer in the surface. This distance corresponds to half of the interatomic plane distance in the $\langle110\rangle$ structure. Figure 3(b) shows the average density profiles in the bulk at the same distance from a layer inside the solid. The $\langle110\rangle$ structure is clearly seen, with the maxima at the corners corresponding to the positions of the Ag atoms that are at the surface. The density peak in the middle of the figure for the bulk density disappears in the case of the surface because this peak corresponds to a contribution from the plane below the considered one.

The spatial distribution of the valence charge density was used to calculate the electronic stopping of the projectile along its trajectory within the local density approximation. As may be seen, the electronic charge density of the Ag$\langle110\rangle$ surface strongly depends on the azimuthal angle, so the electronic stopping power will also depend on the relative orien-

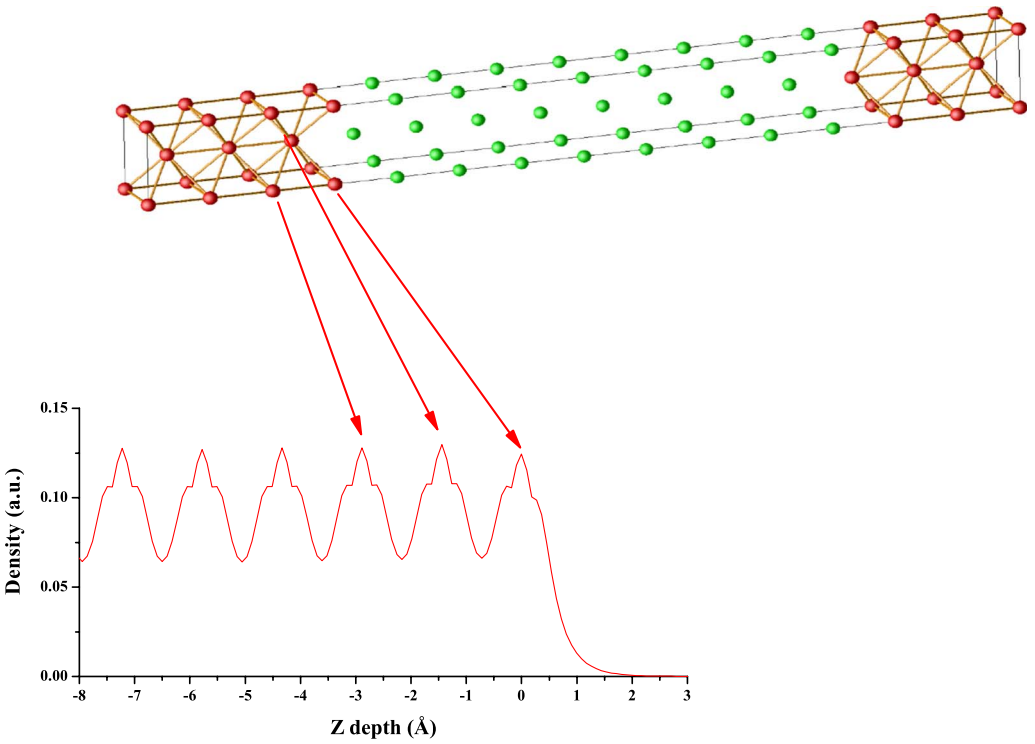

FIG. 1. (Color online) Superlattice used in the calculation of the electronic charge density in the Ag(110) surface. The solid (red) spheres represent the position of the Ag atoms. Gray (green) spheres depict the open spheres. Also shown is the averaged electronic density below the picture (in red).

tation of the surface with respect to the ion azimuthal incidence. It is also clear that information on ion surface distance dependent stopping obtained from scattering experiments assuming an averaged electron density at any given distance from the surface could be unrealistic (see, e.g., [4–11]), although the simulation may yield reasonable results for some scattering configurations.

IV. MODEL CALCULATION

The simulation of particle trajectories is made by solving the Newton equation of motion using the Runge-Kutta method of integration. For comparison we use various potentials in order to describe the interatomic forces between the projectile and the lattice atoms, Lenz-Jensen, Molière, and Ziegler-Biersack-Littmark approaches, which are denoted by V_{lattice}. The expression describing dynamics of the ion is

$$\vec{F}(\vec{r}) = M\frac{d^2\vec{r}}{dt^2} = -\vec{\nabla}V_{\text{lattice}}(\vec{r},\vec{R}) - \vec{\nabla}V_{\text{imag}}(z) + \vec{f}(\vec{v},n(\vec{r})). \tag{1}$$

In this equation, M is the projectile mass; r is the ion position, and R the crystal atom position. V_{imag} correspond to the image potential. The term $\vec{f}(\vec{v},n(\vec{r}))$ corresponds to the friction force arising from the ion-electron interaction and depends on the electron density in a given point of the lattice, $n(\vec{r})$. The features of this friction force are described below.

A. Image potential

If we consider the charge state (positive or negative particle) of the incident particle, we have to consider the image force V_{imag} on the projectile induced by the presence of the projectile charge in front of the metallic surface. This average force is used in the calculation in the approximation of Jones, Jennings, and Jepsen (JJJ) for the surface barrier in a metal [18,19]:

$$V_{\text{imag}}(z) = \begin{cases} \dfrac{1}{2(z-z_0)}\{1-e^{-\lambda(z-z_0)}\}, & z<z_0, \quad \alpha = \dfrac{2U_0}{\lambda} - 1, \\ \dfrac{-U_0}{\alpha e^{-\beta(z-z_0)}+1}, & \text{otherwise}, \quad \beta = \dfrac{U_0}{\alpha}. \end{cases} \tag{2}$$

Here α and β are obtained by fitting $V_{\text{imag}}(z)$ and its derivative at the image plane $z=z_0$. Image potential parameters for the Ag(110) face are obtained by first-principles calculations and using a database of surface-state energies in the metals. These parameters have the following values: $z_0=-1.53$ a.u. is the image plane position; $U_0=1.03$ Ry, and $\lambda=0.96$ [19]. For this system the corresponding jellium edge is $z_j=-1.36$. Figure 4 shows the plotted curves for the image potential and the image force derived from this potential. We also show the projection of the mean electronic density at the surface and the bulk in the XZ plane calculated as described above. The vertical axis is in arbitrary units, and the horizontal axis is perpendicular to the (110) surface and is in atomic units. The

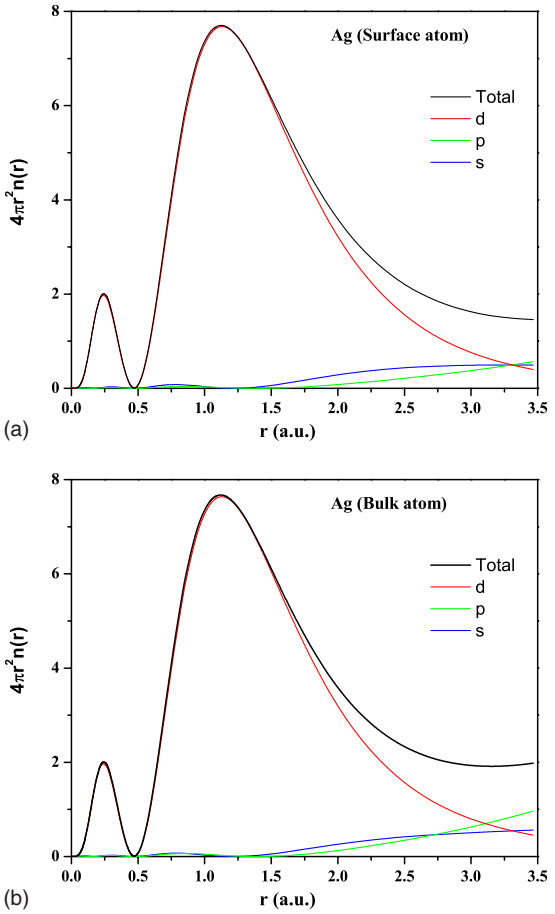

FIG. 2. (Color online) Radial averages for s, p, and d partial charge densities of electrons (multiplied by $4\pi r^2$) as a function of distance from the nucleus in (a.u.) for Ag atoms (a) at the surface and (b) in the bulk.

maxima in the electron density profile correspond to the atomic positions of silver atoms close to the surface.

B. Atomic vibrations

We will also briefly consider the effect of atomic vibrations. Uncorrelated lattice vibrations are introduced assuming that the atoms are allowed to move independently of each other in all directions. There exist several theoretical calculations and experimental approaches in order to obtain the rms vibrational amplitudes at crystalline surfaces [20–22]. Below the third or fourth layers, we use the bulk value given by the tabulated Debye temperature for Ag(110) [23] equal to 225 K, corresponding to 0.09 Å. In the case of Ref. [20], the semiempirical findings are larger than theoretical calculations [21,22]. In our simulations we use a standard Gaussian distribution for the probability of finding the atom at a distance u from its equilibrium position. Here we impose a cutoff for u because it has the practical advantage that very large displacements never occur [24]. Thermal vibrations are considered as static disorder. Also, here we do not consider lattice atom dynamics since a projectile at the energies considered here sees a static, frozen, surface, and bulk along its path.

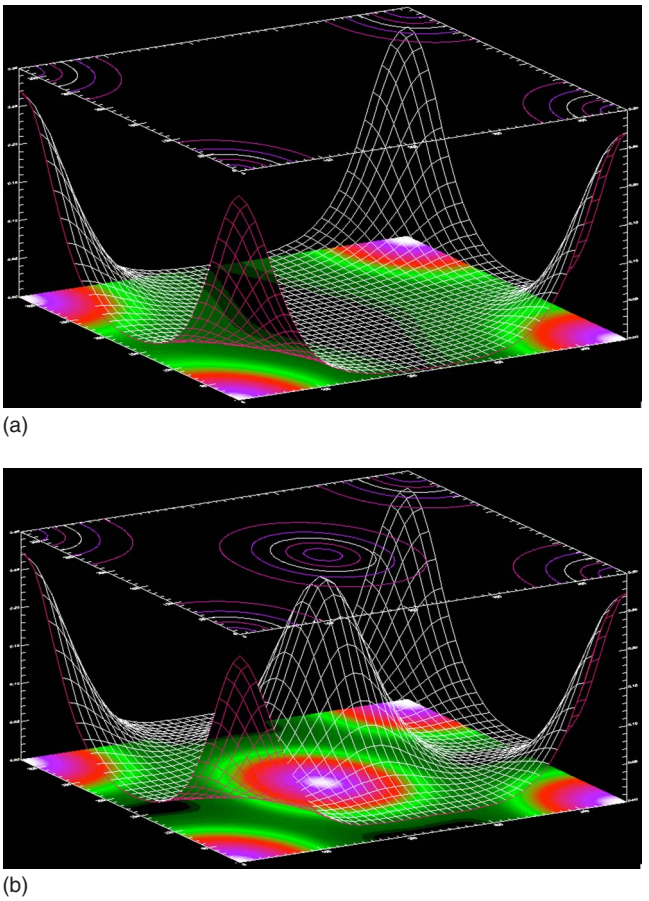

FIG. 3. (Color online) (a) Average charge density profile in the bulk at 0.72 Å of distance from any atomic layer. (b) Average charge density profile at 0.72 Å of distance below the first atomic layer at the surface.

C. Energy loss and threshold effect

The electronic energy loss is included explicitly in the dynamics of the particle using the instantaneous particle energy calculated in a continuous slowing-down process. Also a spread of energy loss determined by the energy loss straggling effect is included. This important parameter is partially responsible for the broadening of the energy loss spectra. The magnitude of the particle energy loss interacting with a homogeneous jellium based on the nonlinear or transport cross-section model is given by [14]

$$\frac{dE}{dx} = -nvv_e\sigma_{\mathrm{tr}}(n) = -Qv. \tag{3}$$

In this equation, n is the electron density, v the ion velocity, and Q is the so-called friction coefficient. The factor σ_{tr} is the transport cross section in terms of phase shifts $\delta_l(n)$, corresponding to scattering of waves with angular momentum l, and is given by the well-known expression

$$\sigma_{\mathrm{tr}} = 2\pi\int_0^{\pi} |f(\vartheta)|^2(1-\cos\vartheta)\sin\vartheta\, d\vartheta, \tag{4}$$

where $f(\vartheta)$ is the scattering amplitude given by

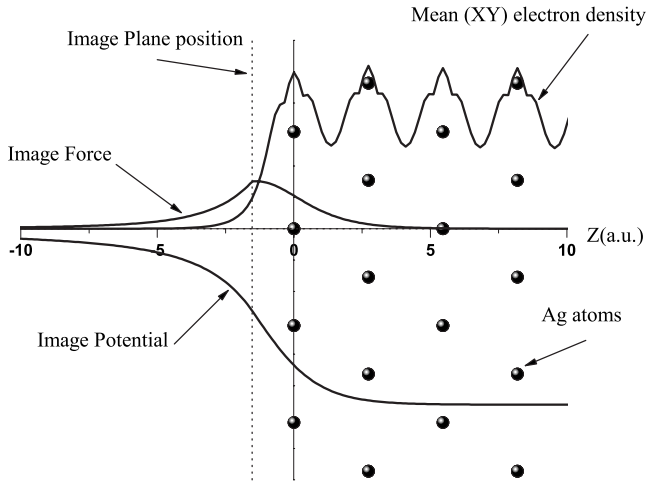

FIG. 4. Image force and image potential profile (vertical axis is in arbitrary units and the horizontal axis is in atomic units). Also shown, is the projected averaged *XY* electronic density in the plane *XZ* and the position of the image plane.

$$f(\vartheta) = \frac{1}{v_F}\sum_l (2l+1)e^{i\delta_l}\sin(\delta_l)P_l(\cos\ \vartheta), \tag{5}$$

where v_F is the Fermi velocity in the center-of-mass reference frame. Phase shifts are determined numerically by solving Schrödinger's equation for the scattering of electrons by a known hydrogenic screened potential and the transport cross section (TCS) approach [12]. This is a self-consistent model to adjust the screening constant and ensure that the Friedel sum rule is satisfied [14]. In a similar way and using the same nonlinear model, we include the quantum fluctuations in the energy loss, the energy loss straggling for low velocities, given by [25]

$$\Omega^2(n) = 3nv^2v_F^2\Delta x\int d\sigma(n,\vartheta)\sin^3(\vartheta/2). \tag{6}$$

In this relationship, $d\sigma$ is the differential scattering cross section, obtained also from the phase shifts $\delta_l(n)$, and Δx is the path length.

Several linear and nonlinear theoretical calculations of the stopping power for slow ions predict a simple proportionality with the ion velocity in the case of metallic targets [1,3]. The origin of this velocity dependence can be traced back to the basic properties of the free electron gas model. However, recent experiments on energy loss of protons in metals like Cu, Ag, Au, and Pd have shown significant deviations from this prediction for ion energies below about 5 keV [26–28]. This behavior was explained as arising from band structure effects [13]. Indeed the electronic structure of transition metals strongly deviates from that systems, like Al. In the latter systems there is a typical parabolic density of states (DOS) where the free-electron gas model applies and yields Eq. (3) for the velocity dependence of the stopping power. Previous experiments have shown that this dependence is well satisfied for Al, Sb, and Bi, but not for transition elements like Cu, Ag, Au and Pd [29,30]. Experiments for energy loss of protons and deuterons in channeling conditions through

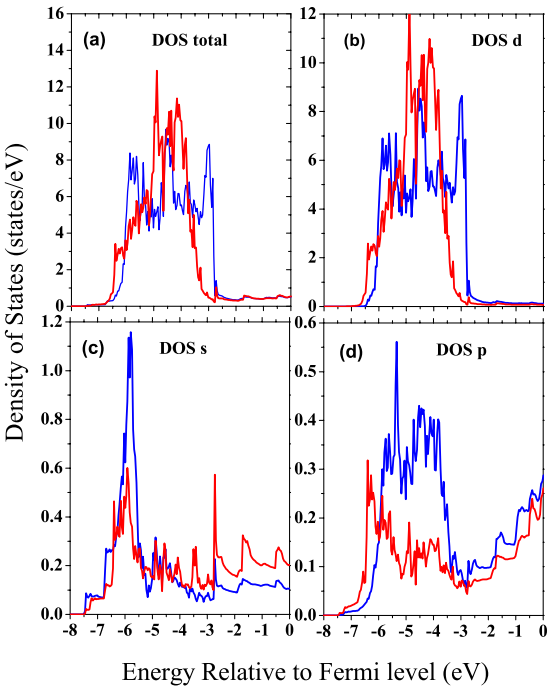

FIG. 5. (Color online) Density of states for bulk (blue line) and surface (red line) for Ag(110) system: (a) total density of states (b) *d* density of states, (c) *s* density of states, and (d) *p* density of states.

monocrystalline thin films of gold have been performed recently [31]. In that work experimental results provide clear and detailed evidence of the departure from the velocity proportionality and they show a transition between two regimes in the energy loss processes: one corresponding to a high-velocity regime, from 0.5 to 1.0 a.u., and a second regime of very low velocities, below 0.1 a.u. Additionally, in that work the authors present a simplified model that describes the strong influence of the material's electronic structure on the ion energy loss through the so-called threshold effect. Another recent experimental work [32] gives also additional evidence for the nonlinear dependence of the energy loss for protons obtained using a different geometry, where they use TOF low-energy ion scattering. This overall evidence leads us to consider and include a "threshold effect" for protons in surface scattering calculations onto a crystalline Ag target.

In order to clarify details about the electronic band structure for Ag(110), in Fig. 5 we show *ab initio* calculations of the total and partial densities of states for bulk and surface: (a) total density of states, (b) density of states for *d* electrons, (c) density of states for *s* electrons, and (d) density of states for *p* electrons. These densities of states were obtained using the same *ab initio* approach for the spatial electron density, tight-binding (TB) LMTO, described in Sec. III. The partial DOS for *s* and *p* electrons does not show a free-electron-like character, or a parabolic behavior as in the aluminum case. Furthermore, the *s* state shows a localized band close to the bottom of the band. The *p*-state behavior is somewhat similar to that of the *d* states.

The model for the threshold effect that we applied in this work is an improved model with respect to the one used in a previous paper [13] and the analytical one presented by

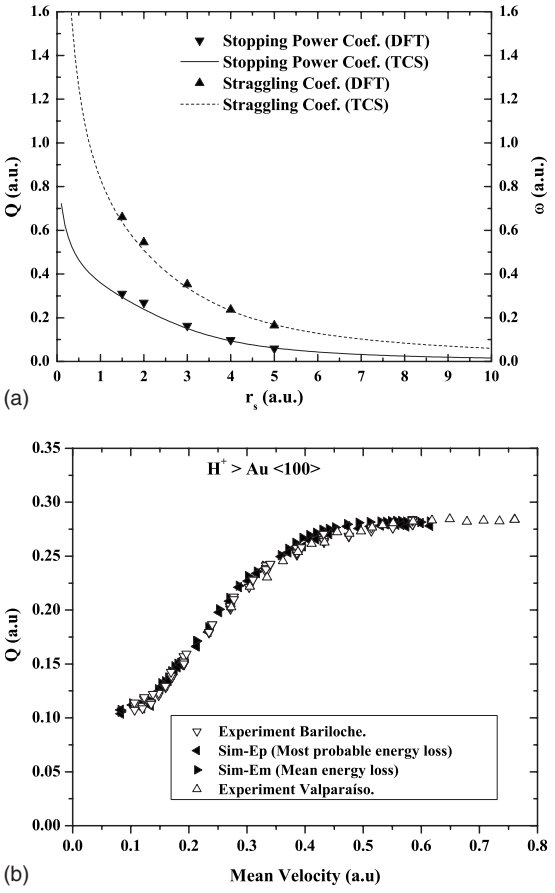

FIG. 6. (a) Energy loss and energy loss straggling parameters Q and ω [see Eq. (13)] as a function of the electron density parameter r_s: solid and dashed curves, respectively, in the TCS approach [12], and up and down triangles, DFT [3] approach for energy loss straggling and energy loss, respectively. (b) Experimental friction coefficient as a function of velocity for protons transmitted through monocrystalline Au(100) film, from the Bariloche setup (down open triangles) and from the Valparaíso setup (up open triangles). Together with these data, we show the calculated coefficient using our dynamical simulation for protons in a single-crystal gold. Data correspondence is the following: left solid triangles are the most probable energy loss, and right solid triangles are the mean energy loss obtained from the simulated energy loss distribution in transmission geometry.

Valdés *et al.*[30]. Here we maintain basic and fundamental ideas about the threshold effect, but with some additional considerations. In the previous work we have considered the threshold effect for d electrons, while the s and p electrons were considered as free. Because of the above-mentioned characteristics of the density of states for s and p electrons for Ag, we also include here the threshold effect for these states too.

In a previous work of Valdés *et al.* [30], in describing the threshold effect, Au was considered to be monovalent and the electronic configuration for a free Au atom is $5d^{10}6s^1$. However, according to TB-LMTO calculations, the electronic configuration for Ag atoms in the bulk is $4d^{9.51}5s^{0.72}5p^{0.77}$ and at the surface is $4d^{9.56}5s^{0.69}5p^{0.44}$.

In order to introduce the threshold effect in the excitation of *valence-band* electrons, we use the fact that we know the contribution from s, p, and d electrons to the charge density in a given point of the lattice $\vec{r}$. We consider the total electronic density at $\vec{r}$, $n_{\mathrm{loc}}(\vec{r})$, and an effective local electron density $n_{\mathrm{eff}}(\vec{r})$. Regarding the total electron density, the corresponding electron states in the solid are localized and bound (according to the appropriate density of states), and so the creation of an electron-hole pair is achieved only if the projectile loses a minimum of energy, ΔE, in a binary collision. This energy threshold is the difference between the Fermi energy and the energy of the electronic state of the involved electrons. Then, only a fraction of the electrons of the local electron density $n_{\mathrm{eff}}(\vec{r})$ at the instantaneous projectile position $\vec{r}$ can be excited and contribute to the stopping power and to the energy loss straggling of the particle.

In the binary collision approximation, the energy transfer is [33]

$$\Delta E(\vartheta) = v v_r (1 - \cos\,\vartheta). \tag{7}$$

Here, ϑ is the scattering angle of the electrons in the laboratory system and v_r is the relative velocity between electron velocity and ion velocity. To estimate the threshold energy, we use an average energy transfer depending on the electron density:

$$\langle \Delta E \rangle = v \langle v_r(n) \rangle \beta(n). \tag{8}$$

Here we consider the relative velocity in the limit $v \ll v_F$, $\langle v_r(n) \rangle = v_F$, where $v_F = (3\pi^2 n)^{1/3}$. The factor $\beta(n)$ is defined as the average value of $1-\cos\,\vartheta$ over the normalized cross section function:

$$\beta(n) = \frac{\int |f(\theta)|^2 (1 - \cos\,\vartheta) d\Omega}{\int |f(\theta)|^2 d\Omega}. \tag{9}$$

The mean energy transfer is then compared with the bandwidth of the local density of states (LDOS). We use the fact that the probability distribution of energies of the electrons in a given point is given by the normalized LDOS. Therefore, if $\langle \Delta E \rangle$ is larger than the bandwidth, all the electrons of the corresponding band can be excited. On the other hand, when $\langle \Delta E \rangle$ is a fraction of the bandwidth, only the fraction of electrons lying between $E_F - \langle \Delta E \rangle$ and E_F in the LDOS can be excited. By this method, not all valence electrons can be excited in a given interaction, and therefore only a fraction of the valence electrons contribute to the stopping. This effect is enhanced at lower proton velocities, where only a reduced fraction of valence electrons of the system contribute to the stopping power. The calculated electronic LDOS indicates the way in which the electron energies are distributed. Usually the DOS are normalized in such a way that the integral up to the Fermi level gives the total number of electrons, but we can also normalize the DOS such that the integral up to the Fermi level is unity, and in this way, the integral of the DOS between two arbitrary energies gives the percentage of the electrons having their energies in that range. Therefore the DOS can be interpreted as the probability distribution of the electronic energies in the system. In our model we as-

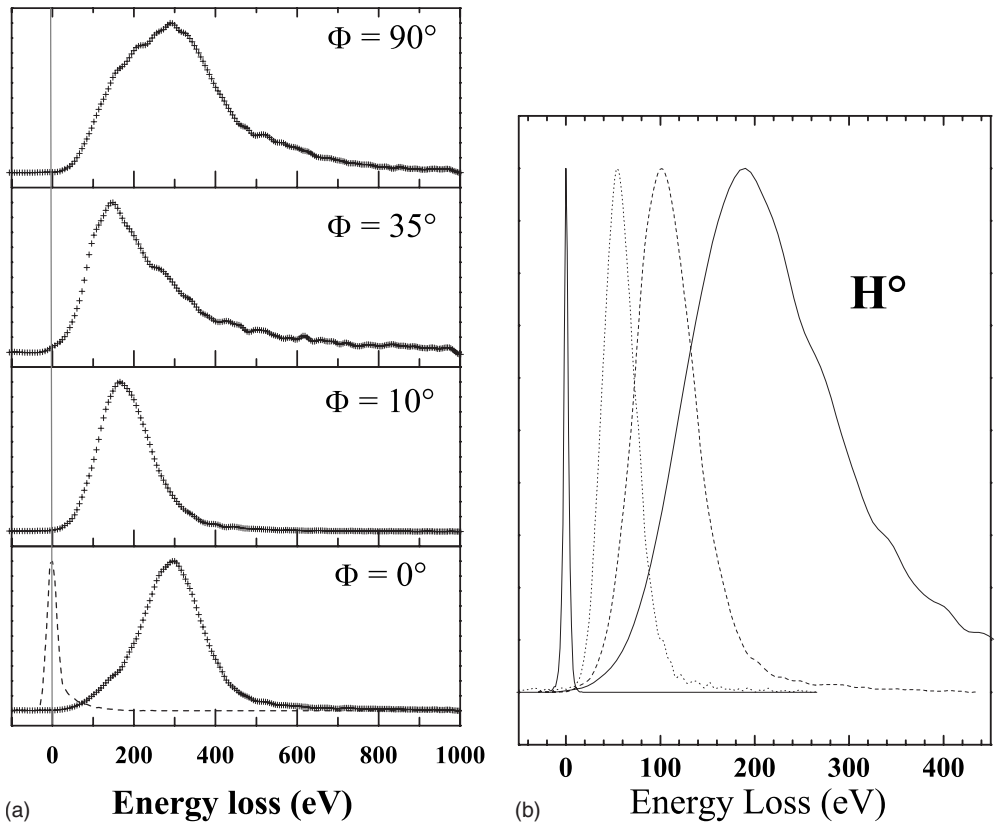

FIG. 7. (a) Experimental energy loss spectra of incident 4 keV hydrogen scattered through 7° along different azimuthal directions on clean Ag(110). The dashed line in the bottom panel shows the incident beam profile. (b) Energy loss spectra for 7° scattering in a random direction of incident hydrogen for 1, 2, and 4 keV. The incident beam profile is shown for hydrogen for 1 keV.

sume that the same probability distribution is also valid locally in the frame of the local density approach.

Then, for a given point in the lattice, the local electron density is given by

$$n_{\mathrm{tot}}(\vec{r}) = n_s(\vec{r}) + n_p(\vec{r}) + n_d(\vec{r}) \tag{10}$$

and the *effective* electron density is given by

$$n_{\mathrm{eff}}(\vec{r}) = n_s(\vec{r}) \int_{\varepsilon'}^{\varepsilon_F(r)} g_s(\varepsilon) d\varepsilon + n_p(\vec{r}) \int_{\varepsilon'}^{\varepsilon_F(r)} g_p(\varepsilon) d\varepsilon + n_d(\vec{r}) \int_{\varepsilon'}^{\varepsilon_F(r)} g_d(\varepsilon) d\varepsilon. \tag{11}$$

Here, $g_s(\varepsilon)$, $g_p(\varepsilon)$, and $g_d(\varepsilon)$ are the l-projected density of states of the system and we define $\varepsilon' = \varepsilon_F(r) - \langle \Delta E \rangle$, where ε_F is the Fermi energy of the system and $\langle \Delta E \rangle$ given by Eq. (8). Summarizing, the energy loss and the energy loss straggling are both a function of the particle velocity and of "the effective electron density." Consequently, the energy loss and energy loss straggling quantities can be written as

$$\frac{\delta E}{\delta x} = \vec{f}(\vec{v}, n_{\mathrm{eff}}(\vec{r})) = -Q(n_{\mathrm{eff}}, v)v, \quad \Omega^2 = \omega(n_{\mathrm{eff}}, v)\delta x v^2. \tag{12}$$

Thus, the coefficients Q, the *friction coefficient*, and ω depend on the excitation spectra of the electrons and the ion velocity. In Fig. 6(a) we show these parameters as a function of r_s, without regarding the velocity dependence. The parameter r_s is the one-electron radius defined through the free electron gas density model as $r_s = (3/4\pi n)^{1/3}$. In Fig. 6(a) we show calculated coefficients for stopping and straggling using the TCS model and Friedel sum rule as mentioned previously, corresponding to the solid line and dotted line, and the result of more elaborate calculations using the DFT formalism [3]. In this model we use the TCS approach because we need an extended range of r_s, useful for taking into account the spatial inhomogeneity distribution of the electron density.

In order to show the features of our model and the velocity dependence of the energy loss , we have done simulations for protons and deuterons in transmission through single crystal gold in the ⟨100⟩ direction. In that plot we show the experimental data obtained by two independent laboratories (Bariloche and Valparaíso). Our calculation for the friction coefficient is shown in the Fig. 6(b) together with recently published experimental results[31]. Good agreement may be seen between experiment and simulation data.

This plot [Fig. 6(b)] is the best way to visualize the threshold effect. At high velocities the friction coefficient behaves as theory predicts and is velocity independent. In this velocity range using Eq. (3), we can say that the mean electron density probed by the projectile is around 0.058 28 a.u. ($r_s = 1.6$). This value corresponds to 7.75 electrons per atom participating in the stopping process, so they can be

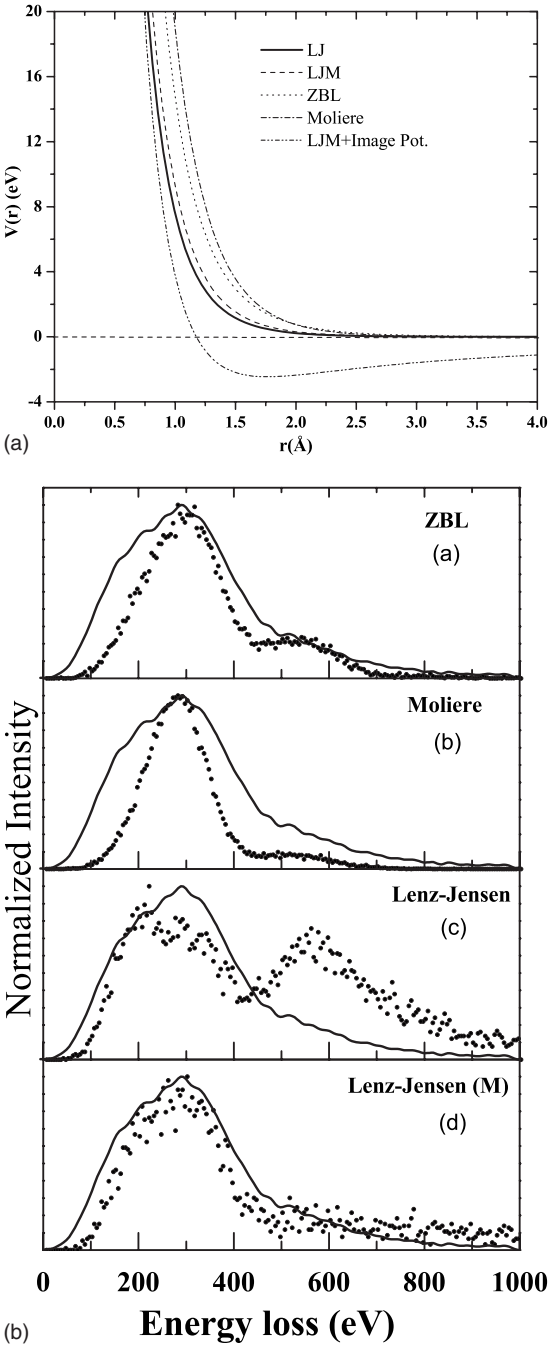

FIG. 8. Panel (A): interatomic distance (Å) dependence of the ZBL, Molière, Lenz-Jensen (LJ), modified LJ, and modified LJ plus image potentials (eV); see Eq. (2) for the image potential. Panel (B): dots represent the simulated energy loss distribution for 4-keV protons incident 90° azimuthal direction for the following potentials (a) ZBL; (b) Molière, (c) LJ, and (d) LJ (modified) potentials. In all these calculations with different potentials, we include the image potential. Solid lines correspond to the experimental energy loss distribution.

considered as free electrons. For velocities below 0.45 a.u., the effect begins to be appreciable and the friction coefficient depends strongly on the ion velocity. At very low velocities, below 0.15 a.u., we can observe a new saturation zone, where the projectile probes a mean electron density of

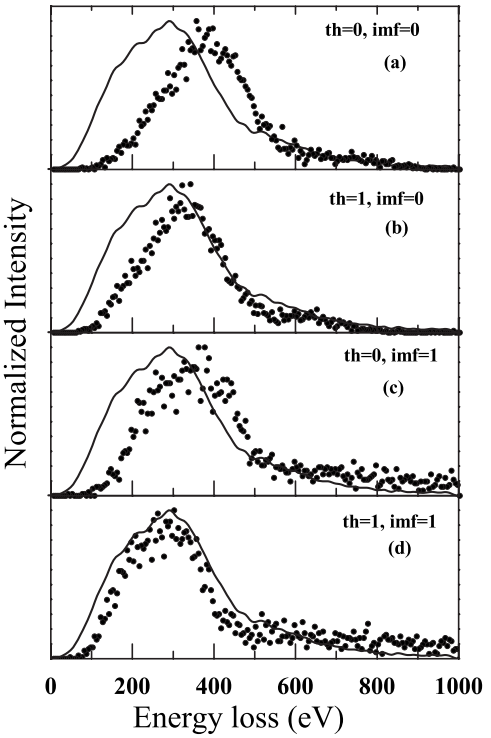

FIG. 9. In this plot we show the energy loss distribution for 4-keV protons incident at 90° regarding image and threshold effects. The solid line in the figures corresponds to the experimental spectrum.

0.00435 a.u. (r_s=3.8), corresponding approximately to 0.58 electrons per atom.

V. EXPERIMENTAL AND THEORETICAL RESULTS

In this section we describe the experimental data and the calculations of energy loss distributions for protons scattered from a Ag(110) surface. These energy distributions are obtained for different azimuthal incident directions. We will first show the experimental results and thereafter study the characteristics of the calculated energy loss distributions along the main azimuthal directions and in random direction. Finally, we do a comparison between experimental and simulated data.

A. Energy loss distributions: Experiment

Figure 7 shows hydrogen energy loss spectra measured as a function of the crystal azimuth for a 4-keV incident ion energy. One can see that in general the energy loss spectra are fairly narrow for a "random" scattering direction (not corresponding to the main low-index crystallographic directions; see, e.g., the spectrum for scattering in the 10° direction) and broaden for scattering along the channeling directions. One can note that the spectra for the channeling directions appear to be composed of roughly two components. Thus at 4 keV the spectrum for the zero-degree azimuth has a maximum at 300 eV and a small shoulder at about 180 eV. For the 90° azimuth the spectrum has a maximum at about 300 eV and a larger shoulder at about 180 eV.

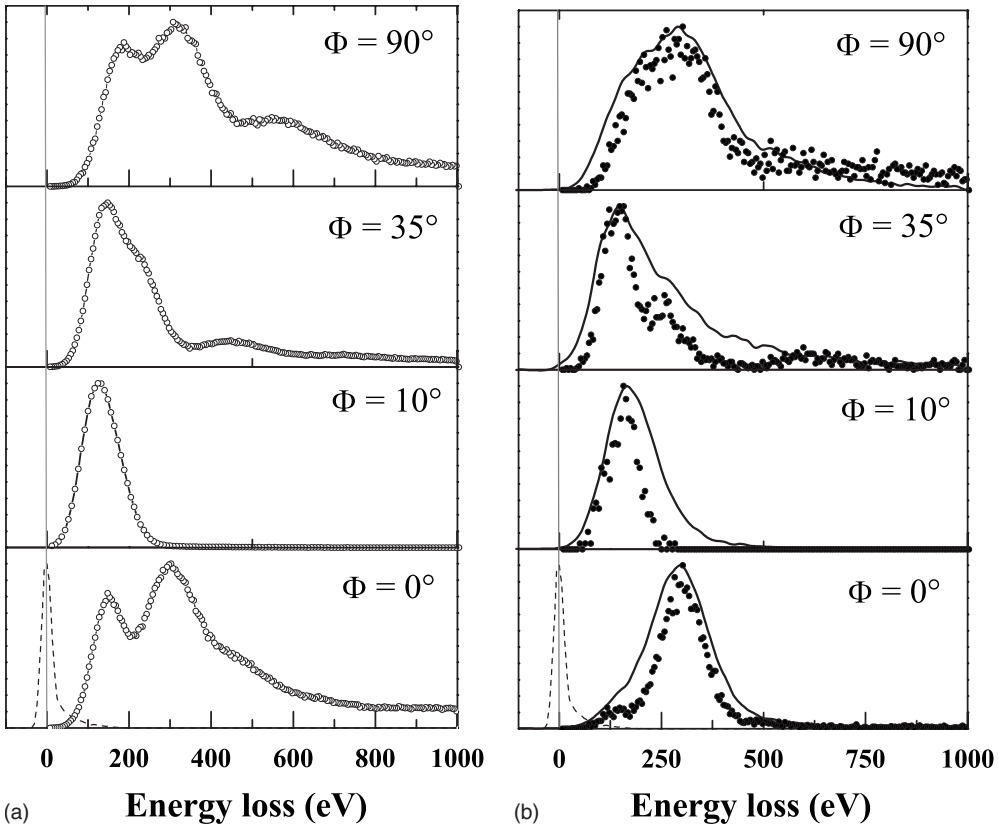

FIG. 10. Calculated energy loss distribution for protons at 4 keV for different azimuthal directions as indicated in each panel. In panel (a) are plotted the total energy loss distributions corresponding to all particles scattered off the surface. In the panel (b) we show the energy loss distributions for "detector-selected" particles (solid circles) and the experimental data (solid lines).

For random scattering (e.g., at the measured angles of 10°, 23°, or 53°), the energy loss is about 180 eV. Rapid changes in the energy loss spectra occur when the azimuthal angle is changed in the vicinity of the channeling direction [11], and for large deviations from the channeling direction the shape of the spectrum tends to the shape for random scattering.

The energy losses for various outgoing charge states were found to be essentially the same (see also Maazouz *et al.* [34]). This was also the case for *incident* H^+ and H^-. The energy losses are found to increase with increasing energy as illustrated in Fig. 7(b) for the random scattering case. The energy dependence for various azimuthal orientations will be discussed later below.

B. Energy loss distributions: Simulations

In this section we show the results corresponding to simulations of the energy loss distributions for protons with incident energies ranging between 1 and 4 keV, with a 3.5° incident elevation angle, for different azimuthal directions: 0°, 90°, and random directions. The energy loss distributions of those particles are "detected" at 3.5° in the scattering plane using a virtual "detector"; we will call this distribution "selected." The dimensions of this "detector" are similar to the experimental one. The energy spread in the incident beam, which is comparable to the experimental one, is also considered in these simulations (see Fig. 7).

We can also count all the scattered particles (2π solid angle), and the energy loss distributions thus obtained are called "total." The simulations were done for several thousand trajectories for each incident energy and angular parameters. The output data files contain either final positions and velocities or the positions and velocities for particle trajectories as a function of time.

Using our computational code, we can easily obtain trajectories, energy loss distributions, and angular distributions of all the scattered particles. In particular, we can obtain energy loss distributions for particles traveling above the surface or inside the solid and analyze the contribution of those particles with different trajectories to the total energy loss spectrum. Here we shall show general results of energy loss distributions and examples of characteristic trajectories as a function of the azimuthal orientation of the target.

1. Choice of interatomic potential, threshold, and image potential effects

It should be pointed out here that when protons approach the surface they are efficiently neutralized. The resulting hydrogen atoms can then be converted into negative ions by resonant electron transfer as discussed in detail by Maazouz *et al.* [34]. A rigorous description of energy losses must include the effect of the electron transfer and include the effect of the image force on the particle trajectories when considering ionic movement. At present, this is difficult to perform and the exact charge state of the ion near the surface remains problematic. In the following we therefore present calculations in which we consider first two extreme cases in which

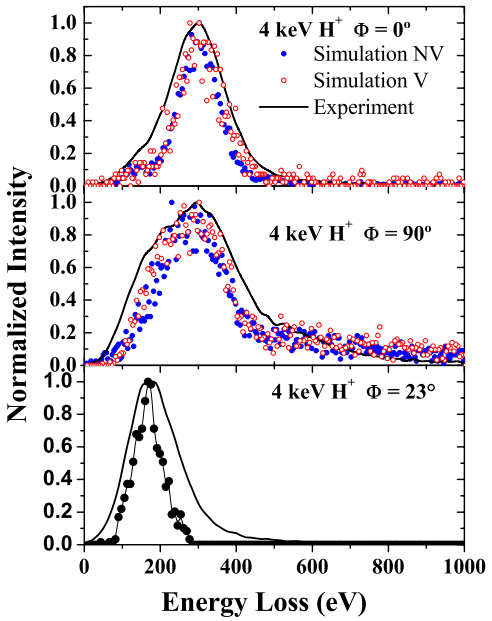

FIG. 11. (Color online) Simulated energy loss distributions for a 4-keV proton beam incident at 0°, 90°, and 23° azimuthal angles and 3.5° elevation angle compared with their respective experimental energy loss distributions. The effect of including or not the atomic vibrations is shown for 0° and 90° azimuth directions.

the image force (i) is not included, (ii) is included up to the image plane, and (iii) up to the end of the trajectory. The first case corresponds to no neutralization or neutralization in the incoming path very far from the surface. The second and third cases corresponds to strong image potential modifications of the trajectory and should be overestimations of its effect, since proton neutralization should occur efficiently over a range of distances before reaching the image plane. Some negative ion formation and destruction should also occur, and therefore we also include case (iii).

On the other hand, in the inelastic stopping power calculations we consider that the proton moves as screened particle in an inhomogeneous free electron gas, so the stopping depends on the electron density along its trajectory. According to the analysis done by Arista [35], slow protons in metals behave as free particles dressed by a screening cloud of conduction electrons for velocities smaller than about 1 a.u. This conclusion is backed by full-size band structure calculations from Vargas *et al.* [35]. At higher velocities ($v > vF$) bound states of electrons around protons appear, and at the same time the coupling between the projectile and the target weakens. Therefore it is a good approximation to consider only one charge state during the simulation; that is, we assume that the stopping power can be calculated considering that there always is a screened proton. However, the phase shifts vary during the proton trajectories as they depend upon the local value of the electron density.

We shall first discuss the shape of the energy loss distributions for different interatomic potentials. The model potentials used in these calculations were Ziegler, Biersack and Littmark (ZBL), Molière, and Lenz-Jensen (LJ) [36], and LJ potentials with a small modification to the screening length following the O'Connor-Biersack approach [37], which we call the LJM potential. Here we use the Thomas-Fermi screening length given by $a=\frac{0.88534a_0}{(\sqrt{Z_1}+\sqrt{Z_2})^{2/3}}$, which was multiplied by a factor of 1.07. This modification gives the best agreement with the experimental energy loss distribution as shown in the Fig. 8, plot (d) in panel (B). In our case for grazing scattering the long-range part of the interatomic potential is important; see, e.g., Ref. [38]. This is because in our case the perpendicular velocity with respect to the surface determined by

$$E_\perp = E_0 \sin^2(\vartheta), \tag{13}$$

where E_0 is the incident energy and θ is the elevation angle, is small. Thus this energy value is approximately 15 eV for 4 keV of incident energy and 3.5° incident angle. The behavior of these potentials as a function of internuclear distance is illustrated in Fig. 8 [panel (A)].

As shown in the Fig. 8 [panel (B)], the experimental energy loss distributions using these potentials, and including threshold effect and image force, show an asymmetric shape where in some cases shoulders appear. This secondary structure arises from different contributions to the particle energy loss where trajectories explore different electron densities and travel at different distances with respect to the surface atomic planes before they reach the detector (see below). It is noteworthy that *all potentials give a most probable energy loss (peak maximum) close to the experimental result*.

In Fig. 9 we compare the energy loss distributions obtained using the LJ-modified potential, considering the image force and threshold effects. We show the energy loss distribution for 4-keV protons incident at 90°. We show the results for the cases when the image potential is (imf=0) not included and included (imf=1) up to the end of the trajectory. Also shown is the effect of the threshold effect (th=0 or th=1). A third case is considered here, where we include the image potential up to the image plane in the ingoing trajectory. In this case no particles are detected in the specular position of the elevation angle of the detector—i.e., at 3.5°; instead of this, we obtain particles at 4.2°. There is not much difference in shapes for the two cases [(b) and (c) in Fig. 9] of inclusion of the image potential.

Inclusion of the image potential results in more or less significant modifications of the shape of the energy loss distributions, including the appearance of a long tail at large energies. As will be discussed below, the large energy tail is due to particle penetration into deeper layers of the surface. The greatest overall change corresponds to the case of the LJ potential. The position of the most probable energy loss is reduced somewhat for the LJ potential and appears as a hump at large energies. Changing the screening length to this potential we obtain good agreement with the experiment. The inclusion of the threshold effect leads to a lowering of the energy loss by about 100 eV and is thus an important correction in agreement with the results of transmission experiments on the similar Au case.

It the absence of an accurate treatment of electron transfer phenomena and image potential along the proton trajectory, it is at present difficult to identify the correct interatomic potential that should be used. None of the potentials yield a

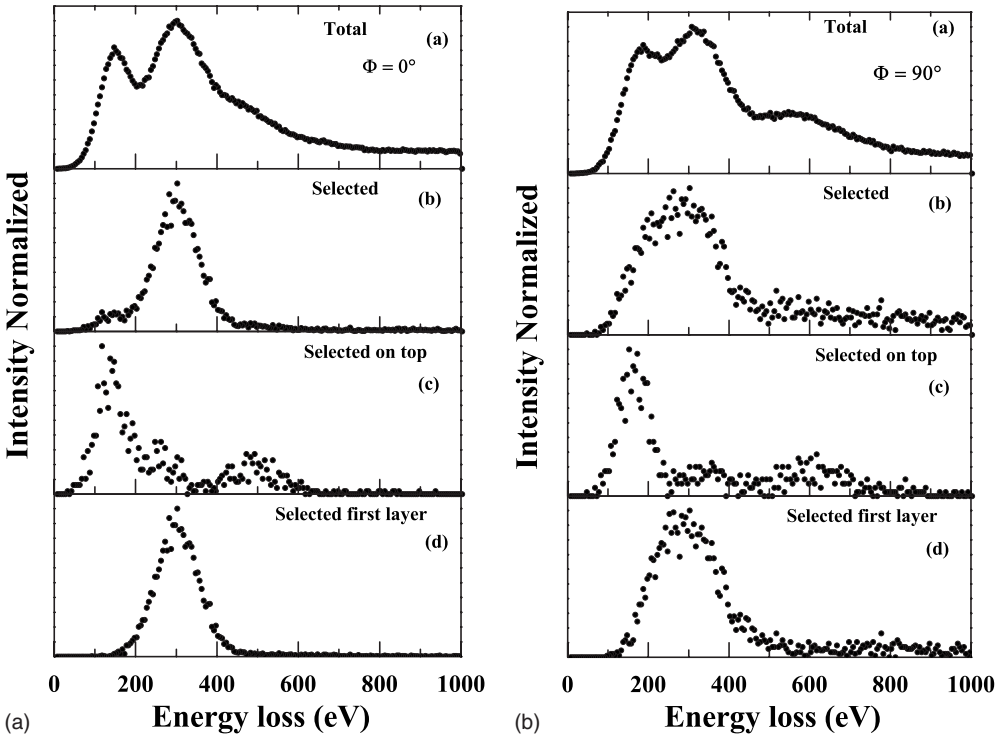

FIG. 12. Energy loss distribution for 4-keV protons incident at 0° [panel (A)] and 90° [panel (B)] directions and detected in the same direction: (a) total energy distribution, (b) selected distribution at 3.5°, (c) selected particles coming from on top of the surface, and (d) selected particles coming from the first interlayer.

very good agreement with the overall *shape* of the experimental energy loss spectrum. Interestingly the best agreement with the experimental energy loss distributions is found using the a modified LJ model potential, which thus presumably best models the effective potential (including image force effects and threshold effect) during scattering. In the following we shall therefore discuss calculations that were done using this potential to illustrate the main aspects of stopping as a function of energy and azimuthal scattering angle.

2. Azimuthal dependence of energy losses

In Fig. 10, panel (a), we show the total calculated energy loss distributions corresponding to protons at 4 keV incident in the azimuthal directions: 90°, 35°, 10°, and 0°, "detected" in 2π. In the right panel (b), we show the calculated energy loss distributions that have been "detector selected" and compared with the corresponding experimental results of Fig. 7. In the right panel, lines represent the experimental data and circles the calculated distributions. These calculations were done using LJ interatomic potential model, with threshold effect.

As may be seen, the overall characteristics of spectra for the different azimuthal orientations can be reproduced. As mentioned, there were no experimental data corresponding to the "total" energy loss distribution.

3. Effect of thermal vibrations

Finally, in Fig. 11, we show a comparison of the calculated energy loss distributions with the experimental ones with and without the inclusion of atomic vibrations. This is illustrated only for the 0°, 90°, and 23° directions, since simulations become extremely lengthy. Thus, the spectrum without atomic vibrations corresponds to a calculation with

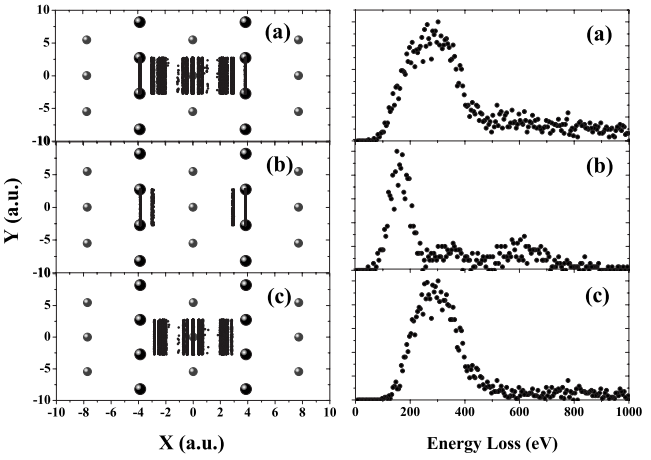

FIG. 13. Sketch of the Ag(110) surface (left panel), black solid circles are Ag atoms of the first layer, gray solid circles correspond to Ag atoms of the second layer. Small black points indicate the initial position of the particles on top of the surface that, after scattering, reach the "small detector". In some cases these merge into lines. The incident projectile is in the 90° azimuthal direction (a) The initial position of all the particles, (b) the initial position of particles that travel on top of first layer, and (c) the initial position of particles that will travel between the first and second layers. Also shown (right panel) are the corresponding energy loss distributions.

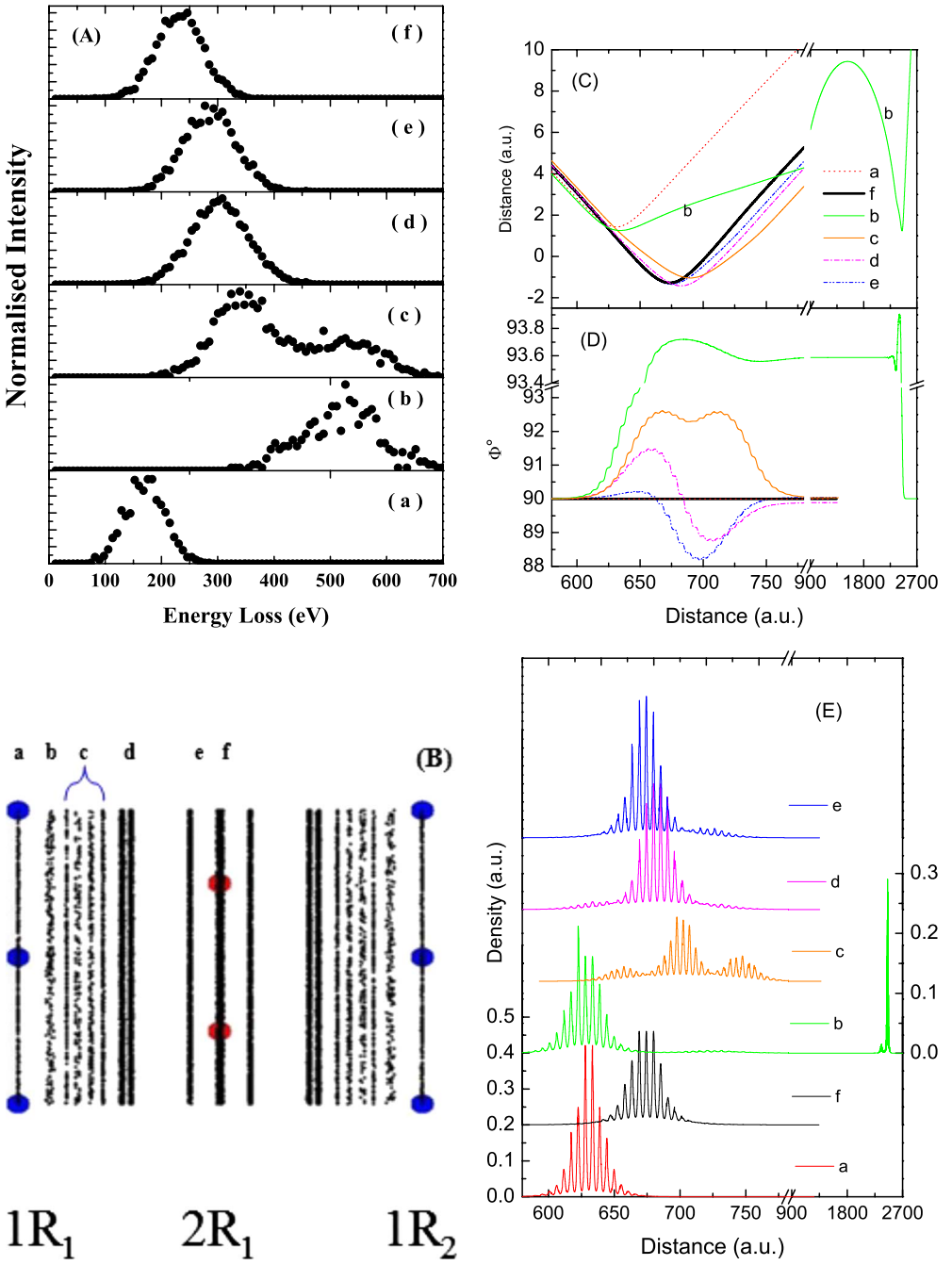

FIG. 14. (Color online) (a) Energy loss distribution for 4-keV protons incident at 90° azimuthal angle and 3.5° elevation angle, corresponding to the initial impact points shown in panel (b). (c) Examples of trajectories (atom surface distance dependence) corresponding to the different regions $a-f$ in panel (b). (d) Azimuthal angle variation along the trajectory for the cases shown in panel (c). Electronic density "seen" by the ions along the trajectories of panel (c). The vertical scale is the same for all plots except for (b) for which the scale is indicated on the right.

500 000 trajectories while the one with atomic vibrations to about 1 000 000 trajectories. The effect of including atomic vibrations leads an enhancement of the main peak and the shoulder corresponding to those particles traveling on top of the surface tends to disappear or to diminish its intensity. Here we included uncorrelated atomic vibrations in which all atoms move independently. This approach presumably gives an upper limit to this effect. A more refined approach should include "correlated" atomic vibrations as discussed in, e.g., [39].

4. General characteristics of detector-selected spectra

Here we analyze different contributions in the energy loss spectra. An interesting question regards the regions on top and below the surface, explored by the particles, which contribute to different parts of the energy loss distribution.

In Fig. 12 we show the energy loss distribution for 4-keV protons incident along the 0° and 90° azimuthal angles. For these scattering directions, the main contribution to the energy loss spectra comes from particles channeled in the first interatomic layer.

To get a more refined analysis, in Fig. 13 we show a sketch of the Ag(110) surface, where we have added the projected *initial impact positions on the surface* for particles that finally reach the experimental-like, "small," detector and contribute to the final spectrum, with different energy losses. The atomic rows of the first layer are denoted by solid circles while the atomic rows corresponding to the second layer are denoted by crosses. In the left panel, Fig. 13(a), we indicate the initial position of all the particles. Figure 13(b) indicates the initial position of particles that travel on top of the first layer, and Fig. 13(c) indicates the initial position of particles that travel between the first and second layers. The right panel of this figure illustrates the corresponding energy loss spectra. As may be expected, in general, the deeper interlayer space contributes to the tail of high energy losses, due to the high electron density distribution below the surface. Trajectories below the first atomic surface layer contribute to the maximum of the energy loss distribution. Above the surface the trajectories mainly contribute to low energy losses. However, we also observe a high-energy-loss contribution.

A more detailed analysis of the energy losses as a function of trajectory type is presented in Fig. 14 for 90°. The energy loss spectra [panel (A)] corresponding to different trajectory classes labeled $a-f$ in panel (B) are shown. The characteristics of these trajectory classes are further illustrated in panels (C)–(E), in which we show, for some selected trajectories, the atom surface distance dependence, the evolution of the azimuthal angle along the trajectory, and the density "seen" along the trajectory (the plots are drawn along the 90° direction). Note that the oscillations in the density curves correspond to the maxima of electronic density near the atoms along the trajectory. The energy losses corresponding to these trajectories are *a*, 199 eV; *b*, 427 eV; *c*, 317 eV; *d*, 348 eV; *e*, 318 eV; and *f*, 238 eV.

The smaller losses correspond to particles traveling above the first ($1R$) and second ($2R$) layer atoms, for which the trajectories (types *a* and *f*) lie along the initial azimuthal direction. Trajectories $b-e$ are of a *zigzag* type (see also, e.g., [6]) and yield larger energy losses, since the atoms cover a longer distance in regions of higher electron density. In this case the atoms actually travel through subsequent regions of high density, moving close to atomic rows, as may be seen in panel (E). The trajectory *b*, starting near row $1R_1$, corresponds to a special type of "skipping" motion (see, e.g., [40]), where hydrogen first recedes from the surface, traveling at an oblique angle of about 93.5°, and is then attracted back to the surface by the image potential, finally bouncing back in the original direction after a rather long distance. It thus again passes through a region of high electronic density as may be seen in panel (E). The intermediate trajectory changes correspond to passage close to other atomic rows. These are reflected in the tiny secondary "hump" in the electronic density observed at a ca. 750 a.u. distance corresponding to flight above the adjacent top row $1R_2$ of atoms. A similar small hump may be observed more clearly as a step just before the final maximum in the electron density at about 2600 a.u. Sampling of some other trajectories in this region (which, however, did not reach the "small" detector and are not included here) shows examples of multiple hops.

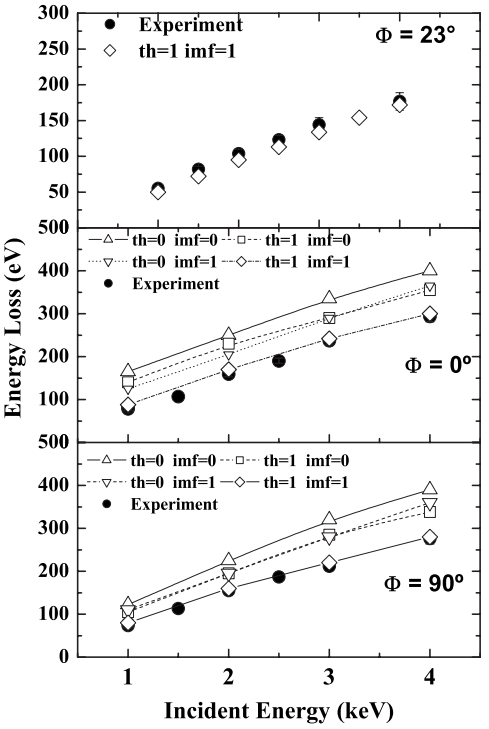

FIG. 15. Most probable energy loss obtained with the simulations compared with the experimental results as a function of the incident energy of the projectiles for main azimuthal angles and random azimuth. Solid circles correspond to the experiment data. Up triangles correspond to calculated energy loss with no threshold effect and no image force. Squares correspond to simulations just including threshold effect. Down triangles correspond to simulations with just image force. Diamonds correspond to the simulation data including the threshold effect and image force.

5. Ion energy dependence of energy losses

In order to get a general picture of the energy loss behavior as a function of the incident energy, the most probable energy loss is plotted as a function of the incident energy in Fig. 15. As mentioned previously, the most probable energy loss is similar for the different potentials discussed above. The calculations shown correspond to the modified LJ potential which appeared to be the best "effective" potential to give good overall agreement with the shape of the experimental energy loss distribution, as described above. We show the trends of the energy loss, with and without the threshold effects and with an without image force effect, for protons incident along the 0° and 90° azimuthal directions. We also show the experiment and calculations for the most probable energy loss for protons incident in a random direction—namely, 23°.

One can see that the simulation including the threshold effect and the image force correctly predicts the general features of the spectrum and is in good agreement with the

position of the maximum of the energy loss spectrum. The threshold effect leads to a roughly 30% decrease in energy loss and results in better agreement with experiment. This is in agreement with earlier investigations in transmission experiments [12] in an Au target.

VI. CONCLUSIONS

This paper presents a joint experimental and theoretical investigation of energy losses in hydrogen ion scattering on Ag(110). The experimental results are compared to calculations of particle energy losses, which combine trajectory calculations and calculations of stopping force. The electronic density of the solid is obtained through first-principles calculations and is then used to determine the stopping force along the particle trajectory. We include a quantum dissipative friction force resulting from the interaction with the valence (s, p, and d) electrons using a nonlinear stopping model, which includes the so-called "threshold effect" as described. We solve the Newton equation of the particle under the influence of the forces due to the nuclei and core electrons and also explore the effect of the force from the surface image potential model. Finally we considered the effect of lattice vibrations.

This description allowed us to study the differences induced by lattice steering effects in the energy loss distributions. The results of these simulations agree quite well with experiment. As opposed to approaches used in earlier works on surface scattering, these simulations in particular allow us to properly take into account the variations of the surface electronic density and hence obtain an accurate description of the energy loss processes for ion scattering along various azimuthal orientations of the target, which are otherwise difficult to describe.

The results of these "all-in-one" simulations appear very satisfying, but one should mention the main problems that should guide further development. The main uncertainties, which we cannot resolve at present, regard knowledge of the exact interatomic potentials and uncertainties in the knowledge of the exact charge state of the particles related to electron transfer phenomena along the approach to the surface, which, because of the existence of the image potential effect, can change the trajectories. Solution of these points relies on a refined analysis of the electron transfer processes, which is not presently available. It is found that the potentials considered predict roughly the same mean (most probable) energy loss, but the overall shape of the spectra can differ considerably. It was noted that the LJ potential would seem to describe best the overall shape of the spectra and thus appeared to be the best "effective" potential (including image potential effects). The effect of uncorrelated atomic vibrations of the surface atoms was considered. This led to a strong change in the contribution from the topmost layer. Inclusion of correlated vibrations as discussed by some authors appears essential in future work to describe this effect in a more realistic manner. A final problem that one should mention regards the possible existence of some steps that could alter the trajectory lengths.

ACKNOWLEDGMENTS

This work was supported by the France-Argentina and France-Chile, ECOS-Conicet, and ECOS-Conicyt collaboration projects; FONDECYT Grants No. 1030175, No. 1071075, and No. 7070175; internal USM-DGIP Grant No. 11.04.23; CONICYT/Programa Bicentenario de Ciencia y Tecnologia (CENAVA) PBCT-ACT027; Millennium Scientific Initiative under Contract No. P-02-054-F; and Millenium Science Nucleus "Basic and Applied Magnetism," P06-022-F (Chile). Also, we gratefully acknowledged useful discussions with N. R. Arista.

[1] J. Lindhard, M. Scharff, and H. E. Schiott, K. Dan. Vidensk. Selsk. Mat. Fys. Medd. **33** (14) (1963).
[2] D. S. Gemmell, Rev. Mod. Phys. **46**, 129 (1974).
[3] T. L. Ferrell and R. H. Ritchie, Phys. Rev. B **16**, 115 (1977); P. M. Echenique, R. M. Nieminen, and R. H. Ritchie, Solid State Commun. **37**, 779 (1981); M. J. Puska and R. M. Nieminen, Phys. Rev. B **27**, 6121 (1983).
[4] A. Garcia-Lekue and J. M. Pitarke, Phys. Rev. B **64**, 035423 (2001); M. Alducin, V. M. Silkin, J. I. Juaristi, and E. V. Chulkov, Phys. Rev. A **67**, 032903 (2003); J. E. Miraglia and M. S. Gravielle, *ibid.* **67**, 062901 (2003).
[5] A. Niehof and W. Heiland, Nucl. Instrum. Methods Phys. Res. B **48**, 306 (1990); A. Närmann, W. Heiland, R. Monreal, F. Flores, and P. M. Echenique, Phys. Rev. B **44**, 2003 (1991).
[6] A. Robin, W. Heiland, J. Jensen, J. I. Juaristi, and A. Arnau, Phys. Rev. A **64**, 052901 (2001).
[7] A. Robin, J. Jensen, D. Osterman, and W. Heiland, Nucl. Instrum. Methods Phys. Res. B **193**, 568 (2002).
[8] K. Kimura, M. Hasegawa, and M. Mannami, Phys. Rev. B **36**, 7 (1987).
[9] H. Winter, C. Auth, A. Mertens, A. Kirste, and M. J. Steiner, Europhys. Lett. **41**, 437 (1998); H. Winter, J. I. Juaristi, I. Nagy, A. Arnau, and P. M. Echenique, Phys. Rev. B **67**, 245401 (2003).
[10] A. Arnau and P. M. Echenique, Phys. Scr. **677**, T49 (1993).
[11] L. Guillemot, E. Sánchez, and V. A. Esaulov, Nucl. Instrum. Methods Phys. Res. B **212**, 20 (2003).
[12] P. Vargas, J. E. Valdés, and N. R. Arista, Phys. Rev. A **53**, 1638 (1996).
[13] J. E. Valdés, P. Vargas, and N. R. Arista, Phys. Rev. A **56**, 4781 (1997); J. E. Valdés, P. Vargas, L. Guillermo, and V. A. Esaulov, Nucl. Instrum. Methods Phys. Res. B **B256**, 81 (2007).
[14] S. Lederer and H. Winter, Phys. Rev. A **73**, 054901 (2006); M. S. Gravielle, M. Alducin, J. I. Juaristi, and V. M. Silkin, *ibid.* **76**, 044901 (2007).
[15] O. K. Andersen and O. Jepsen, Phys. Rev. Lett. **53**, 2571 (1984); O. K. Andersen, O. Jepsen, and D. Gloetzel, in *Highlights of Condensed Matter Theory*, edited by F. Bassani, F.

Fumi, and M. P. Tosi (North-Holland, New York, 1985); O. K. Andersen, O. Jepsen, and M. Sob, in *Electronic Band Structure and Its Applications*, edited by M. Yussouff, Lecture Notes in Physics (Springer-Verlag, Berlin, 1987).

[16] O. K. Andersen, Z. Pawlowska, and O. Jepsen, Phys. Rev. B **34**, 5253 (1986).

[17] V. Esaulov, L. Guillemot, O. Grizzi, M. Huels, S. Lacombe, and Vu Ngoc Tuan, Rev. Sci. Instrum. **67**, 135 (1996).

[18] R. O. Jones, P. J. Jennings, and O. Jepsen, Phys. Rev. B **29**, 6474 (1984).

[19] N. V. Smith, C. T. Chen, and M. Weinert, Phys. Rev. B **40**, 7565 (1989).

[20] B. W. Busch and T. Gustafsson, Surf. Sci. **407**, 7 (1998).

[21] Talat S. Rahman and Zeng Ju Tian, J. Electron Spectrosc. Relat. Phenom. **64-65**, 651 (1993).

[22] Shobhana Narasimhan, Phys. Rev. B **64**, 125409 (2001).

[23] C. Kittel, *Introduction to Solid State Physics* (Wiley, New York, 1995).

[24] M. T. Robinson and O. S. Oen, Phys. Rev. **132**, 2385 (1963).

[25] J. C. Ashley, A. Gras-Marti, and P. M. Echenique, Phys. Rev. A **34**, 2495 (1986).

[26] R. Blume, W. Eckstein, and H. Verbeek, Nucl. Instrum. Methods **168**, 57 (1980); Nucl. Instrum. Methods Phys. Res. **194**, 67 (1982); R. Blume, Ph.D. thesis, München University, 1980; W. Eckstein (private communication).

[27] G. Högberg, H. Norden, and R. Skoog, Phys. Status Solidi **42**, 441 (1970).

[28] J. E. Valdés, G. M. Tamayo, N. R. Arista, G. H. Lantschner, and J. C. Eckardt, Nucl. Instrum. Methods Phys. Res. B **73**, 313 (1993).

[29] J. E. Valdés, C. Parra, J. Díaz-Valdés, C. D. Denton, C. Agurto, F. Ortega, N. R. Arista, and P. Vargas, Phys. Rev. A **68**, 064901 (2003).

[30] J. E. Valdés, C. Agurto, F. Ortega, P. Vargas, R. Labbe, and N. R. Arista, Nucl. Instrum. Methods Phys. Res. B **164**, 268 (2000).

[31] E. A. Figueroa, E. D. Cantero, J. C. Eckardt, G. H. Lantschner, J. E. Valdés, and N. R. Arista, Phys. Rev. A **75**, 010901(R) (2007).

[32] S. P. Chenakin, S. N. Markin, E. Steinbauer, M. Draxler, and P. Bauer, Nucl. Instrum. Methods Phys. Res. B **249**, 58 (2006).

[33] L. de Ferrariis and N. R. Arista, Phys. Rev. A **29**, 2145 (1984).

[34] M. Maazouz, A. G. Borisov, V. A. Esaulov, J. P. Gauyacq, L. Guillemot, S. Lacombe, and D. Teillet-Billy, Phys. Rev. B **55**, 13869 (1997)

[35] N. R. Arista, K. Dan. Vidensk. Selsk. Mat. Fys. Medd. **52**, 595 (2006); P. Vargas and N. E. Christensen, Phys. Rev. B **35**, 1993 (1987); P. Vargas, H. Kronmuller and M. C. Bohm, J. Phys. F: Met. Phys. **16**, L275 (1986).

[36] W. Eckstein, *Computer Simulation of Ion-Solid Interactions*, Springer Series in Material Science, Vol. 10 (Springer-Verlag, Berlin, 1991).

[37] D. J. O'Connor and J. P. Biersack, Nucl. Instrum. Methods Phys. Res. B **15**, 14 (1986).

[38] H. Winter and A. Schüller, Nucl. Instrum. Methods Phys. Res. B **232**, 165 (2005).

[39] T. Okazawa, F. Takeuchi, and Y. Kido, Phys. Rev. B **72**, 075408 (2005); D. J. Martin, Surf. Sci. **97**, 586 (1980).

[40] K. J. Snowdon, D. J. O'Connor, and R. J. Macdonald, Phys. Rev. Lett. **61**, 1760 (1988).